Received: 17 February 2025 | Revised: 24 March 2025 | Accepted: 30 March 2025

DOI: 10.1111/jace.20570

Journal of the American Ceramic Society

SPECIAL ISSUE ARTICLE

The effect of organic additive on electrochemical fabrication of microstructured electrode for reverse electrodialysis

Eunji Kwon[1] | **Donghyun Lee**[2] | **Insoo Choi**[1,2]

[1]Department of Energy and Chemical Engineering, Kangwon National University, Samcheck, Gangwon-do, Republic of Korea

[2]Department of Energy and Mineral Resources Engineering, Kangwon National University, Samcheck, Gangwon-do, Republic of Korea

Correspondence
Insoo Choi, Department of Energy and Chemical Engineering, Kangwon National University, Bldg. 4, Room #224, 346 Jungang-ro, Samcheok, Gangwon-do, 25913, Republic of Korea.
Email: ischoi@kangwon.ac.kr

Abstract

For reverse electrodialysis (RED) to be effectively scaled up and commercialized, it is essential to develop an electrode system that is more active, stable, and cost-effective. In this study, additive-assisted electrodeposition was utilized to fabricate a Pt/Ti electrode. Trisodium citrate (TSC) was selected as a leveling additive, and its impact on the reduction behavior of the Pt precursor and the fabricated electrode was investigated. The addition of TSC shifted the reduction potential of the Pt ion negatively due to ligand stabilization, which suppressed the nucleation and growth of the Pt deposit. A surface-enlarged, small-grained, and uniform Pt over-layer with high coverage was confirmed through FE-SEM and XRD analysis. The largest electrochemical surface of the Pt/Ti electrode with 9% TSC enhanced surface utilization and decreased charge transfer resistance. The citrate in TSC donates electrons to Pt through metal-ligand charge transfer, increasing the electron density of Pt and facilitating the redox reaction at the electrode. The RED single cell with the Pt/Ti electrode from 9% TSC produces 0.88 W/m^2 of power density and demonstrates the long-term operation of the RED stack.

KEYWORDS

additive, electrode, electrodeposition, leveler, reverse electrodialysis, trisodium citrate

1 | INTRODUCTION

As industrialization accelerates, the global demand for energy continues to rise annually. This increased demand has led to heightened consumption of fossil fuels, which has resulted in a surge in greenhouse gas emissions and exacerbated global warming.[1] According to a report by the International Energy Agency, carbon dioxide emissions are projected to reach 37.4 Gt by 2023, with a trend that shows a continuous increase each year.[2] In light of climate change and the finite nature of fossil fuels, transitioning to renewable energy sources is crucial.

Among the renewable energy sources, salinity gradient power (SGP) generation, a form of ocean energy, is distinguished by its stability and sustainability, with notably minimal load fluctuations. Moreover, SGP is believed to possess the highest potential output among renewable sources, with estimates around 2.6 TW.[3–5] When seawater and freshwater are mixed, up to approximately 2.76 MJ of energy can be harvested per 1 m^3 of freshwater, depending on the salinity gradient.[6,7] Current research on SGP primarily focuses on two main technologies: pressure-retarded osmosis (PRO) and reverse electrodialysis (RED).[8] PRO generates electricity by driving a turbine through the osmotic pressure difference created when seawater and freshwater are separated by a semi-permeable membrane.[8,9] RED utilizes a Donnan potential derived from the salinity gradient

across an ion exchange membrane (IEM) between seawater and freshwater. This electrochemical potential acts as the driving force for producing electricity via a redox reaction that occurs at the electrodes, aided by a circulating rinsing solution.[10,11] RED is regarded as more promising due to its simpler operating conditions, streamlined system design, and higher energy conversion efficiency.

Pilot-scale RED projects have been conducted in Italy, South Korea, and the Netherlands.[12–15] In Italy, a project utilized seawater and brackish water as feed solutions, incorporating 125 stacks with a total IEM area of 48 m^2, and it generated 40 W.[13] On Jeju Island, South Korea, another project, using wastewater and seawater, featured 1000 stacks and a total IEM area of 250 m^2, resulting in a power output of 95.8 W.[14] In the Netherlands, a 50 kW RED plant was constructed in the Afsluitdijk region, covering an area equivalent to two soccer fields, employing real seawater and freshwater sources.[15] Not only are pilot-scale demonstrations of RED important, but laboratory-scale research focusing on the fundamentals and performance enhancements is also crucial. The RED system generates energy through selective ion movement and comprises several primary materials, each of which significantly impacting the performance and efficiency of RED. The RED system comprises four main components[16–20]: an IEM that utilizes the ion concentration difference between seawater and freshwater to facilitate ion movement and generate voltage,[21–28] a spacer to maintain optimal ion flow,[29–32] an electrolyte (e.g., seawater or freshwater),[33,34] and an electrode to conduct and generate current through electrochemical reactions.[35–38] Recent laboratory-scale studies primarily focus on mitigating membrane contamination and enhancing durability,[39,40] and improving the electrode system. Importantly, the electrode plays a crucial role in determining the efficiency of RED, making advancements in electrochemical properties and structural design of the electrode more significant.[41]

The electrodes used in RED have evolved from Pattle's copper electrode[17] and Jagur-Grodzinski 's zinc electrode.[20] However, these reactive electrodes pose challenges in RED, such as the need for periodic replacement of the electrolyte redox solution and current reversal. Consequently, inert electrodes with uniform redox couples are preferred for RED applications. Common materials for these electrodes include metal oxides like Ru/Ir, noble metal-coated Ti mesh (e.g., Pt), and carbon-based electrodes. For example, Pt/Ti,[35–38] carbon plate,[42] Ru-Ir/Ti, graphite,[43] and Ti/Ru/IrO_2-Ta_2O_5 or Ti/RuO_2-IrO_2 anodes paired with Ni cathodes were introduced.[18,44] The state-of-the art electrode system, Pt/Ti, is favored due to its excellent electrochemical properties and corrosion resistance under various reaction conditions.

Given the rarity and expense of Pt, it is advisable to minimize its use in the fabrication of Pt/Ti. Among the fabrication methods, electrochemical deposition (ED) is notable for its simplicity, controllability, and processability. It facilitates the formation of a thin catalyst layer, which enhances surface utilization and reduces fabrication costs. The physical properties of the catalyst layer can be easily adjusted by controlling deposition parameters such as solution composition, temperature, potential, and current.[45,46] Unfortunately, the ED technique for Pt on Ti substrates continues to face challenges. Simple galvanostatic or potentiostatic ED results in uneven deposits, reducing both durability and electrochemical reaction efficiency. Moreover, surface cracks occur despite surface pretreatment. Achieving high coverage, optimized thickness, and a large active surface area is essential for enhancing electrode performance and lifespan. Additive-assisted ED could address these issues by modulating reaction kinetics and improving the chemical and structural characteristics of the deposited layer.[47,48]

The additives in ED can be categorized as accelerators, suppressors, and levelers. Accelerators increase the reduction rate of metal ions and promote the formation of the plated layer. Examples include Bis(3-sulfopropyl) disulfide (SPS),[49] and 3-mercapto-1-propanesulfonic acid (MPS).[50] Conversely, suppressors such as polyethylene glycol (PEG),[51] and sodium dodecyl sulfate (SDS) hinder the precursor's reduction and reduce the grain size of the deposit.[52] Leveling agents control the current distribution and regulate the deposition rate, ensuring uniformity of the plated layer.[53] In this study, we employed trisodium citrate (TSC), commonly used as a leveler or complexing agent in electrodeposition, for depositing Pt on a Ti substrate. TSC binds strongly to metal ions and maintains the ionic concentration when complexed. Previous studies have shown that TSC enhances the stability of the plating solution, controls the deposition rate effectively, and improves the smoothness and uniformity of the deposit, while reducing defects in the semiconductor process.[54–56] Other leveling agents such as PEG, Janus Green B, and benzotriazole (BTA) can also be a candidate. PEG suppresses dendritic growth of crystal and flattens the surface but requires a posttreatment to remove a residue. BTA is an effective inhibitor for copper-based electroplating, forming a thin protective layer on the metal surface and inducing selective plating. However, not much has been known for its use in electrodeposition of Pt and the reaction mechanism is rather complicate. On the other hand, TSC is cost-effective and nontoxic and decomposes easily. For these reasons, TSC was chosen in this experiment in order to develop an improved Pt/Ti electrode system. However, the extent of metal ion reduction and the characteristics or morphology of the resulting plated layer vary with the

amount of TSC added.[55,56] To the best of the authors' knowledge, no results have been reported for TSC-assisted ED of Pt. Therefore, in fabricating Pt/Ti electrodes with TSC, it is crucial to investigate how TSC addition impacts the deposition mechanism and varies with different TSC concentrations. This study, using TSC as a lever, focused on monitoring the Pt deposition behavior at various TSC concentrations and determining the optimal concentration for developing a highly uniform, surface-enhanced, and electrochemically active Pt/Ti electrode for RED.

2 | MATERIALS AND METHODS

2.1 | Fabrication of Pt/Ti electrodes

Before electrodeposition, the Ti mesh (100 mesh, ASTM standard, Nilaco Co. Ltd, thickness = 280 μm) underwent a three-step pretreatment to eliminate surface impurities and natural oxides. Initially, the mesh was cleansed with 95% ethanol (Daejung) using ultrasonic radiation for 30 min. Subsequently, it underwent acid treatment with 100 μL of HCl (37%, Daejung), followed by rinsing with de-ionized water and another session of ultrasonic radiation. The mesh was then dried in a vacuum oven at 100°C overnight. The Pt/Ti electrode was subsequently fabricated via electrodeposition using a potentiostat (PGSTAT302N, Autolab) in a 3-electrode system. The electrode setup included a saturated calomel electrode (SCE, −0.2412 V vs. NHE) as the reference electrode, the Ti mesh as the working electrode, and a Pt wire (99%, Φ = 1 mm, Sigma-Aldrich) as the counter electrode. The electrolyte for the Pt deposition contained 5 mM H_2PtCl_6 (Sigma-Aldrich) and 0.05 M H_2SO_4 (both Sigma-Aldrich). The as-prepared Pt/Ti electrodes were fabricated with varying concentrations of TSC (3% to 15% by weight, increasing in increments of 3%) added to the electrolyte. For comparison, a Pt/Ti electrode was also prepared without TSC (0% TSC). To determine the optimal deposition current or potential, linear sweep voltammetry was performed on the bare Ti mesh substrate within an electrolyte range containing 0% to 15% TSC, with voltage ranging from 0.9 V to −0.6 V (vs. SCE). Galvanostatic deposition at a specific current density was employed to fabricate the Pt/Ti electrodes.

2.2 | RED system and operation

A RED unit cell was constructed by alternating one anion exchange membrane (AMV-N, Selemion™, thickness = 120 μm) with two cation exchange membranes (CMV-N, Selemion™, thickness = 120 μm). These commercially available membranes, chosen for their permselectivity of Na^+ or Cl^-, are detailed in Table S1.[33,36,40] Rhombic Ti woven spacers (4.2 cm × 5.3 cm, thickness = 200 μm) and Teflon gaskets (thickness = 320 μm) were utilized to ensure uniform fluid distribution. At each end of the aligned IEMs and spacers, two Pt/Ti electrodes were positioned, with all components encased between epoxy endplates. The schematic of the RED unit cell is depicted in Figure 1. The feed water solutions were prepared by dissolving sodium chloride (NaCl, Sigma-Aldrich) into de-ionized water. The study involved testing low-salinity water at a concentration of 0.05 g/L and high-salinity water at 30 g/L. Both solutions were supplied at a rate of 5 mL/min to the RED cell's inlet (Φ = 2.2 mm) and circulated using a peristaltic pump (Masterflex®, Cole-Parmer, Vernon Hills, IL, USA). The generated brackish water was continuously discarded to maintain the salinity ratio during operation and ascertain the maximum power density. The electrode rinse solution comprised 1 M NaCl, 0.05 M $K_4Fe(CN)_6$, and 0.05 M $K_3Fe(CN)_6$ (both from Sigma-Aldrich) and was circulated at 3.6 mL/min in a closed loop.

With low- and high-salinity water introduced to the RED cell, its performance was evaluated using a potentiostat. The OCV of the RED cell was measured 100 s after initiating the equilibration and stabilization process, while the operating voltage was assessed through galvanodynamic operation at a current rate of 0.1 mA/s until voltage decayed to zero. From these measurements, both *j*–V and *j*–P plots were derived. The measurements were conducted thrice, and the results were averaged. In discussions, the average values were presented. Additionally, a prolonged performance test of the RED was performed using identical settings, specifically focusing on electrode durability by monitoring the RED performance under a constant current of 0.9 mA/cm^2 for 18 h.

2.3 | Physicochemical and electrochemical analyses

The microstructure and surface analysis of the electrode were conducted using Field Emission Scanning Electron Microscopy (FE-SEM, Hitachi, S-4800) at various magnification levels. X-ray Photoelectron Spectroscopy (XPS, Thermo, Al Kα, 1486.6 eV) provides insights into the surface chemical composition and bonding characteristics of the as-prepared electrodes. X-ray Diffraction (XRD, Rigaku, Cu Kα, 1.5406 Å) elucidates the crystal structure of the electrodes, scanned from 10° to 120° at a scan rate of 2°/min. To quantify the electrochemically active surface area of the Pt/Ti electrodes, electric double layer capacitance (EDLC) measurements were conducted in a 3-electrode system. The same apparatus used for

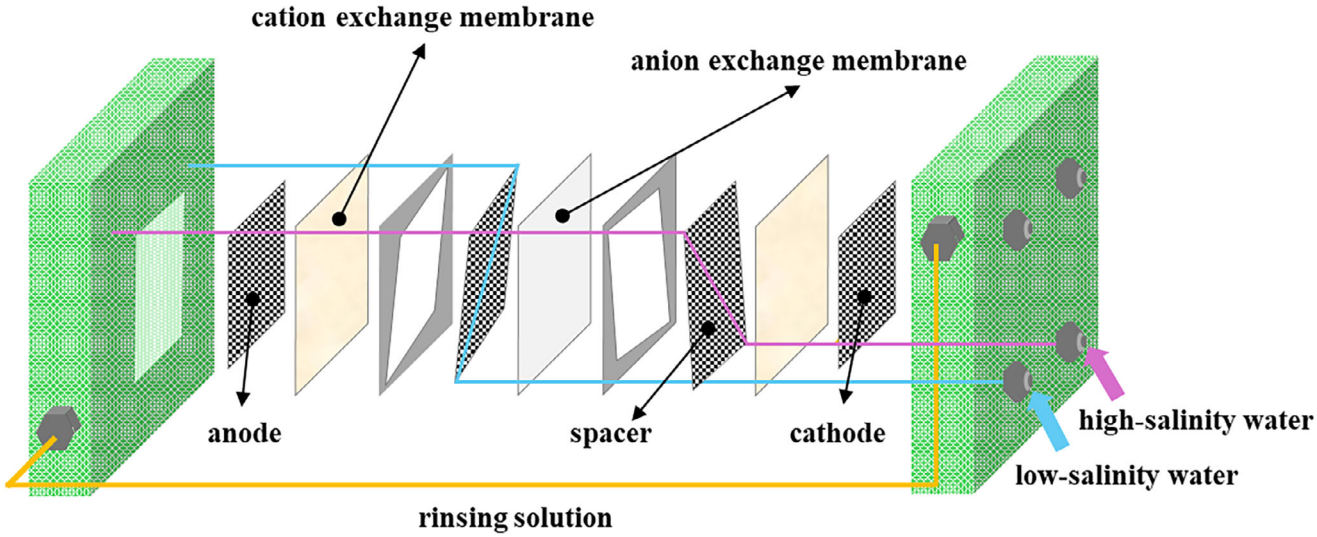

FIGURE 1 Schematic diagram and components of a reverse electrodialysis single cell.

electrodeposition was employed, but the working electrode was Pt/Ti. Cyclic voltammetry for capacitance measurement was performed from −0.35 V to −0.25 V (vs. SCE) at varying scan rates (10–100 mV/s) in 0.1 M KOH(aq) (Daejung). Electrochemical impedance spectroscopy (EIS) was carried out to assess the electrochemical properties and resistance components of the samples. The frequency ranged from 10^6 to 1 Hz, and the amplitude of the AC signal was set at 10 mV. Data were fitted to Randles' equivalent circuit and represented as Nyquist plots to analyze the charge transfer and ohmic resistance.

3 | RESULTS AND DISCUSSIONS

As previously mentioned, linear current sweeping was conducted to observe the electrochemical reduction behavior of the Pt precursor with or without TSC and to identify the optimal deposition current for the fabrication of Pt/Ti electrodes (Figure 2). When the electrolyte devoid of TSC was used, the onset potential for Pt reduction on Ti mesh was approximately 0.85 V_{NHE}. However, the addition of 3% TSC to the electrolyte caused the onset potential to shift negatively by 0.4 V, indicating that the Pt precursor reduction was suppressed. TSC, a well-known complexing agent, is a tricarboxylic acid that dissolves in the electrolyte to form citrate, which complexes with metal cations via its functional groups.[57] Upon coordination, the citrate-Pt^{4+} complex becomes electrochemically stable, and the reduction potential of Pt^{4+} is lowered due to ligand stabilization from the strong interaction between Pt^{4+} and citrate. This strong cathodic polarization of TSC and the resultant negative potential shift have been documented in other studies.[56] The suppression effect of TSC was also

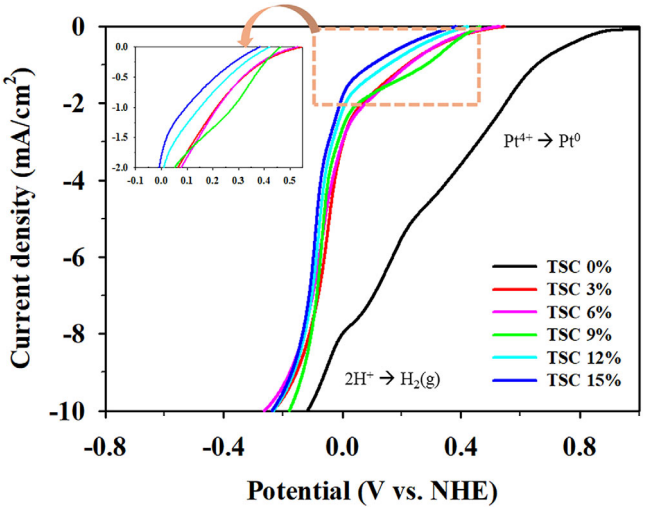

FIGURE 2 Linear sweep voltammograms of electrodeposition of Pt on Ti mesh substrate with TSC concentrations ranging from 0% to 15%.

apparent with 6% TSC. The addition of 9% TSC marginally shifted the onset potential more negatively, yet the reduction current increased slightly. This indicates that although 9% TSC did slow the reduction reaction, it did not suppress the reduction of platinum as significantly as 3% or 6% TSC did. A current plateau with a wide deposition potential window was observed. TSC exhibited a suppressing effect at low concentrations and a leveling effect at concentrations greater than 9%. With 12% and 15% TSC, the onset potential for reduction shifted further negatively, and the reduction current was significantly reduced. This was attributed to the decreased current efficiency associated with increasing concentrations of TSC. Since distinct reduction behavior was observed when the current was

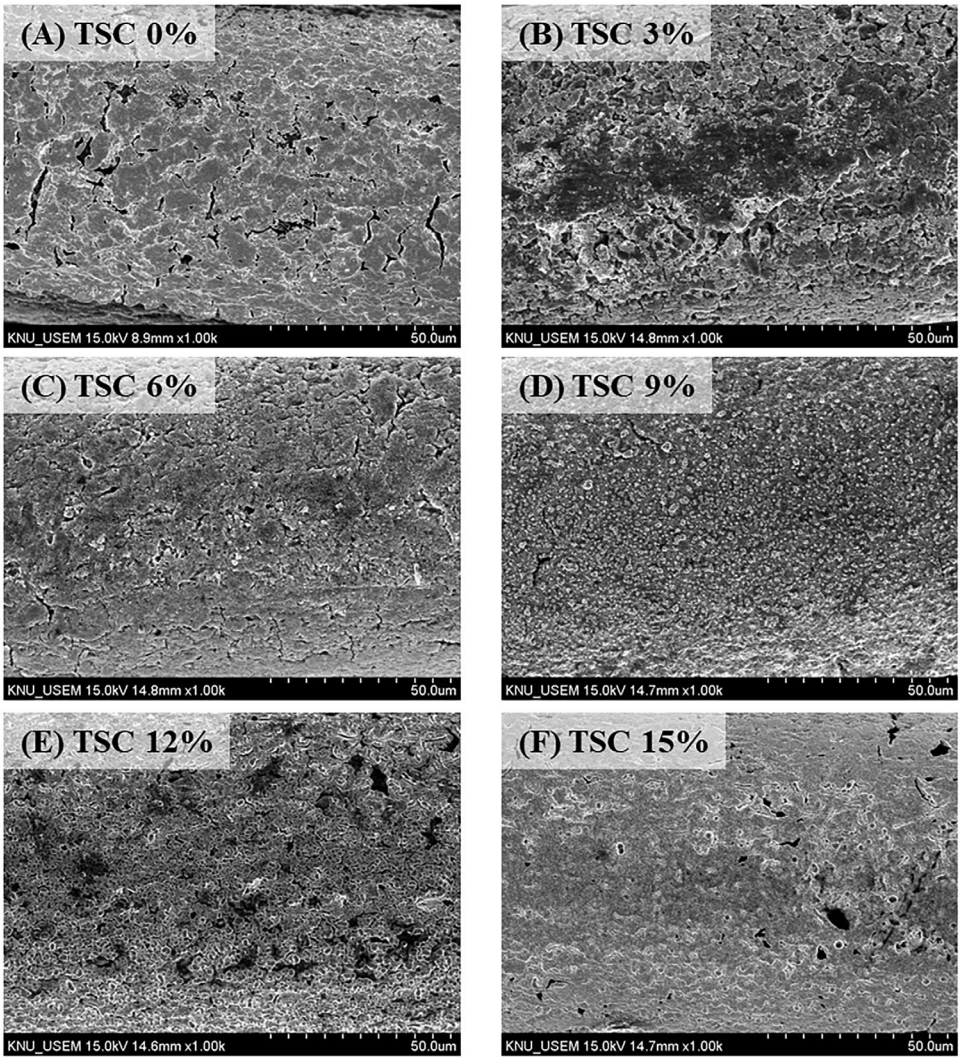

FIGURE 3 Field emission scanning electron microscope images of TSC-based Pt/Ti electrodes: (A) TSC 0%, (B) TSC 3%, (C) TSC 6%, (D) TSC 9%, (E) TSC 12%, (F) TSC 15%.

lower than –0.5 mA/cm^2 and the hydrogen evolution reaction occurred below 0 V, the deposition current was set at –1.3 mA/cm^2 for electrode fabrication.

FE-SEM analysis was conducted to evaluate the surface morphology and deposition profiles of as-prepared Pt/Ti electrodes with varying amounts of TSC (Figure 3A–F). The TSC 0% electrode, produced by the conventional method, exhibited cracks and showed the exposed Ti substrate. These cracks originated from the rough surface of the Ti mesh formed during pretreatment. The TSC 3% and TSC 6% electrodes exhibited improved Pt coverage but still displayed minor cracks and uneven morphology. Notably, the Pt deposit on the TSC 3% electrode appeared less dense, and the quantity of deposit was less pronounced compared to the TSC 0% electrode. The deposits on the TSC 6% electrode were more leveled, yet they still had cracks and pores. Conversely, the TSC 9% electrode featured a fully covered and uniform Pt layer. Furthermore, small-sized crystal grains formed on the surface, a common observation when a leveler is utilized in semiconductor processes. This is because the leveler promotes the nucleation of metal ions on the surface and suppresses excessive particle growth, thereby controlling the grain size to be small.[58] These small and high-density grains create a uniform and smooth surface with a microstructure. This indicates that 9% TSC positively influenced the reduction of Pt on the Ti mesh, effectively suppressed its overgrowth, and developed microstructures on the surface. When more TSC was included, the coverage of the Pt layer appeared to be preserved, but aggregation of Pt particles and a topographical feature with slight height differences were observed. With the highest TSC concentration, numerous holes and pits were seen in the midst of a thick film. It appeared that TSC no longer exhibited a leveling effect when its concentration exceeded 12%. Based on FE-SEM results, the TSC 9% electrode would be the optimal candidate, featuring small

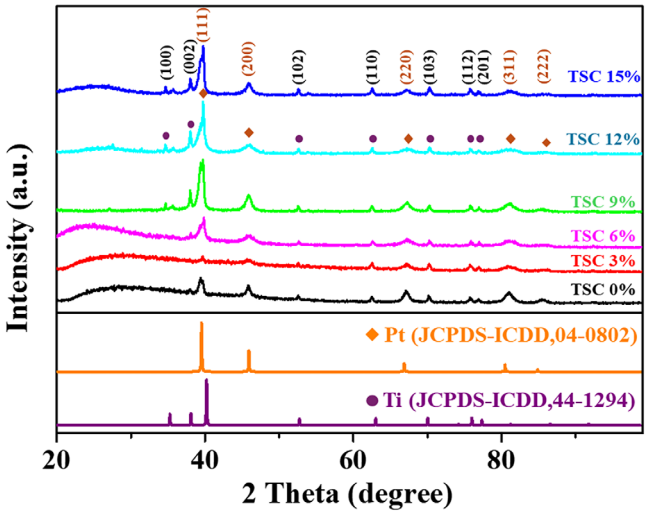

FIGURE 4 X-ray diffraction patterns of TSC-based Pt/Ti electrodes.

grains and high surface coverage with evenly distributed Pt nanoparticles.

The crystalline structure and lattice information of the Pt/Ti electrodes were confirmed via X-ray diffraction, as seen in Figure 4. The diffraction angles and corresponding crystal planes for Pt and Ti were identified according to JCPDS (Pt: no. 04–0802, Ti: no. 44–1294). Increasing the concentration of TSC from 0 to 3 or 6% led to broader characteristic Pt peaks, signifying the formation of small nanoparticles. As further TSC was added, the bulk Pt peaks became distinguishable. The grain size of the Pt deposits was smaller in the TSC 9% electrodes, as evidenced by a reduced full width at half maximum. The crystalline sizes of Pt in all electrodes were calculated using Scherrer's equation and ranged from 5.0 nm to 6.4 nm. The XRD results corroborated the earlier FE-SEM data, indicating that small amounts of TSC (3% and 6%) only suppressed the reduction of Pt precursor and did not contribute to the ideal fabrication of Pt/Ti electrodes. The electrodes prepared with 9% or higher TSC exhibited crystalline Pt with optimized grain size and thickness.

After the manufacture of Pt/Ti electrodes and the completion of physicochemical analyses, a RED unit cell was assembled with these electrodes, and its performance was evaluated. The *j*–V and *p*–V curves for RED with Pt/Ti electrodes prepared with varying amounts of TSC are depicted in Figure 5A and B, respectively. The performance metrics of RED, such as open circuit voltage (OCV), maximum power density (p_{max}), and maximum current density (j_{max}), were compiled in Table S2. The RED unit containing the reference Pt/Ti electrode (TSC 0%) demonstrated an OCV of 0.181 V and P_{max} of 0.712 W/m^2. The RED cell with TSC 3% exhibited reduced performance characterized by a significant voltage drop. The OCV and

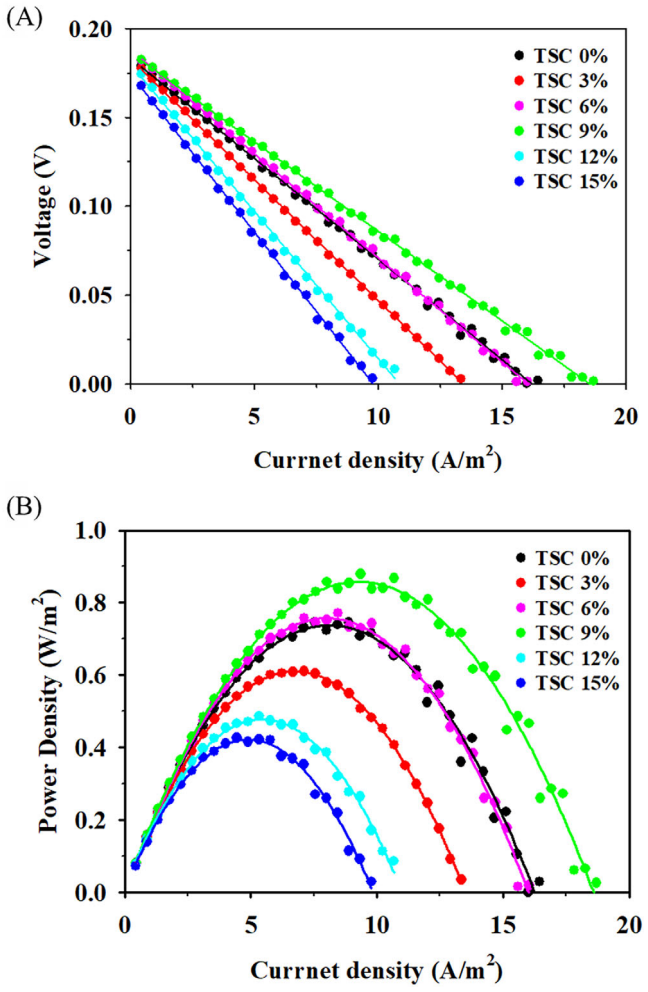

FIGURE 5 Performance of a reverse electrodialysis single cell using TSC-based Pt/Ti electrodes: (A) *j*–V curves, (B) *p*–V curves.

P_{max} for TSC 3% were 0.178 V and 0.624 W/m^2, respectively. As the TSC concentration increased to 6%, the performance of the RED improved, achieving 0.181 V and 0.742 W/m^2. Remarkably, with TSC 9%, the performance further increased to 0.888 W/m^2, representing a 24.7% increase in power density compared to TSC 0%. Previous analyses, including XRD and FE-SEM, suggested that the TSC 9% electrode, characterized by uniform Pt crystallinity, a leveled surface, and extensive surface coverage, could be the optimal electrode material. The RED unit cell results confirmed that the TSC 9% electrode exhibited the highest performance among all tested electrodes. However, with TSC concentrations exceeding 9%, the operation voltage decreased sharply, and the power density was restricted to 0.497 W/m^2. This performance degradation was also observed with TSC 15%. Therefore, it was concluded that electrodes with 12% or more TSC showed lower performance than the reference electrode. The performance decline in the 12~15% TSC range was primarily due to an increase in cell resistance (R_{cell}), as indicated by

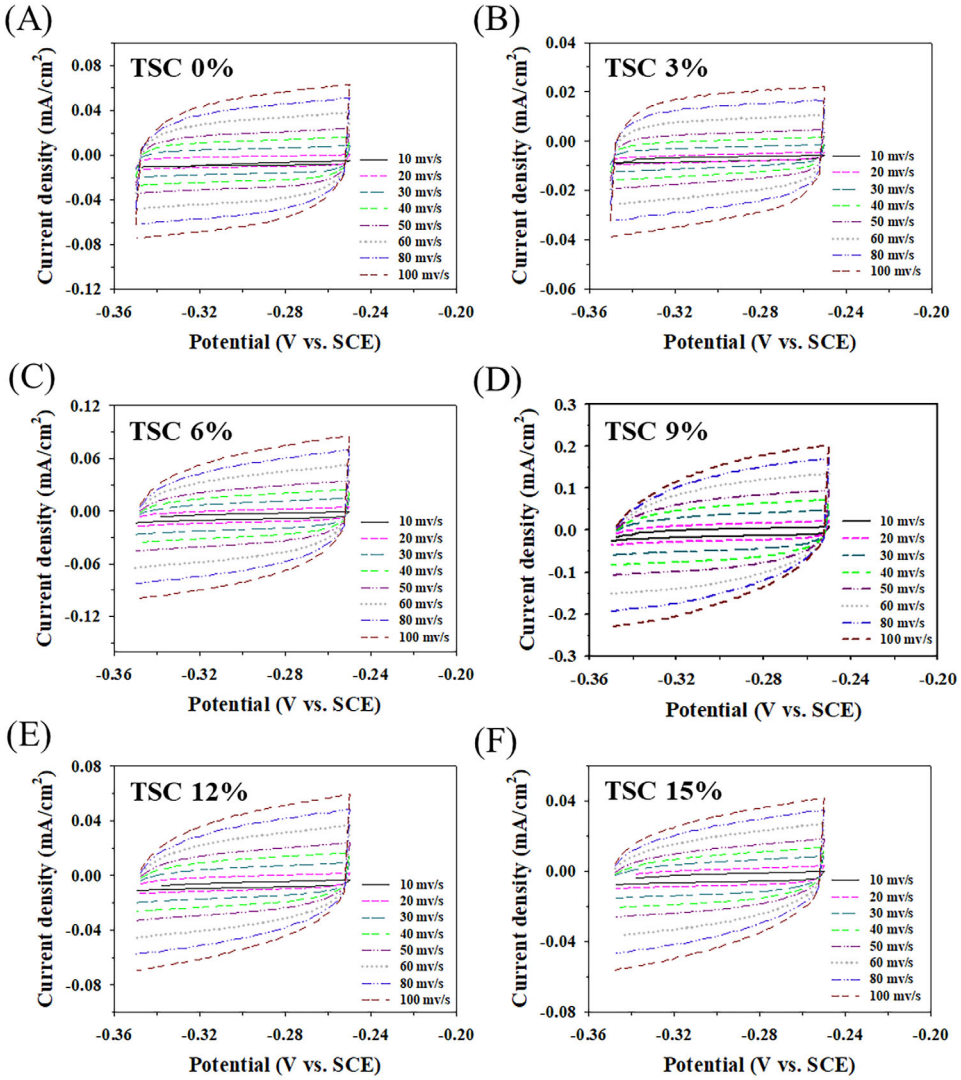

FIGURE 6 Cyclic voltammograms of TSC-based Pt/Ti electrodes in 0.1 M KOH at various scan rates: (A) TSC 0%, (B) TSC 3%, (C) TSC 6%, (D) TSC 9%, (E) TSC 12%, (F) TSC 15%.

the slope of the *j*–V curve. The resistance of the system and its components will be addressed subsequently.

A notable aspect of the performance of RED using TSC-based Pt/Ti electrodes was the observable change in voltage and current, which demonstrated the electrochemical reaction across the electrodes. The electrochemical activity of the TSC-based electrodes determined the reaction kinetics of the rinsing redox pair, thus directly influencing the RED performance. Therefore, we conducted an experiment to elucidate the electrochemical properties of Pt/Ti electrodes, including those incorporating TSC. Initially, to measure the electrochemically active surface area (ECSA) of the electrodes rather than their geometric area, we measured the electric double-layer capacitance as depicted in Figure 6A–F. Cyclic voltammetry was performed on electrodes with 0% TSC and other TSC concentrations by varying a scan rate within a potential region where an electric double-layer was formed. Plotting the half-wave current at a voltage of –0.3 V against the scan rate, the slope of the resulting straight line indicated the charge required to form the electric double-layer per unit area of the electrode. This method allows determination of the specific capacitance of the electric double layer, which reflects the ECSA of the electrode. The results are illustrated in Figure 7. Analysis revealed that the specific capacitance of the TSC 0% reference electrode was approximately 587 μF/cm^2. With an increase in TSC concentration to 3%, the specific capacitance decreased to 266 μF/cm^2, suggesting a decrease in active surface area by nearly half. The reduction was due to exposed Ti mesh and decreased Pt deposition, attributed to the inhibitory effects of TSC as confirmed by FE-SEM and XRD. The specific charge necessary for Pt to form a monolayer (210 μC/cm^2)[59] is significantly higher than that for Ti (45 μC/cm^2), resulting

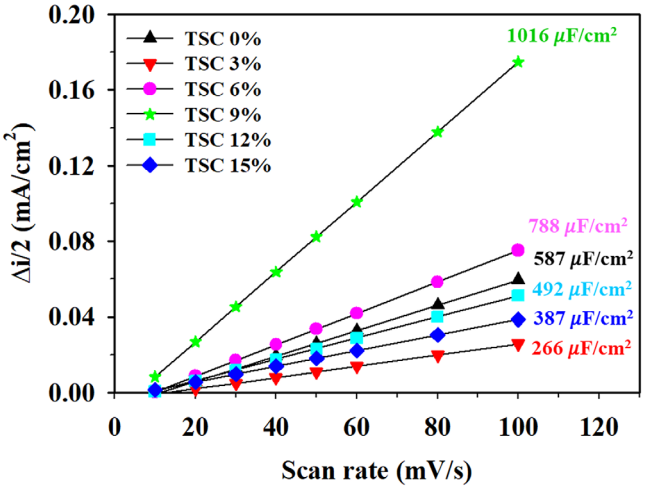

FIGURE 7 Specific capacitance of TSC-based Pt/Ti electrodes plotted against capacitive current from the electric double-layer at different scan rates.

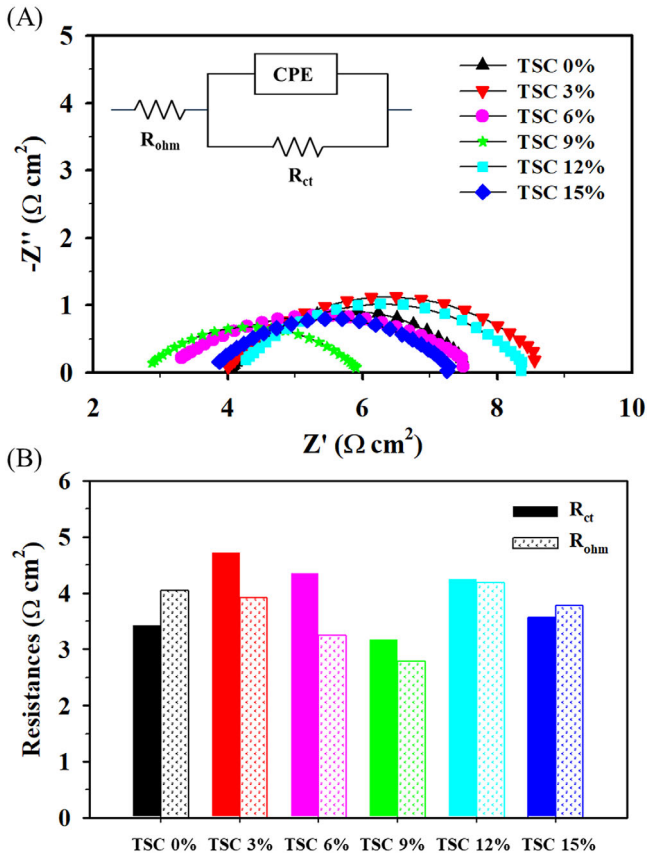

FIGURE 8 Electrochemical impedance spectroscopy of TSC-based Pt/Ti electrodes: (A) Nyquist plots after fitting, (B) charge transfer and ohmic resistance derived from the Nyquist plots.

in a lower total specific capacitance for the double-layer. When TSC concentration was raised to 6%, the specific capacitance increased to 788 μF/cm^2, as more Pt covered the Ti mesh and formed minor cracks, supported by FE-SEM. This suggests that at a concentration of about 6%, TSC ceased to inhibit Pt reduction and began to promote leveling. At 9% TSC, the specific capacitance peaked at 1016 μF/cm^2, 3.8 times higher than that of TSC 0%, indicating a significantly expanded effective active area of Pt capable of catalyzing the rinsing redox reaction. Although the surface coverage of TSC at 6% and 9% was similar, the difference in specific capacitance likely originated from the microstructure developed on the TSC 9% electrode's surface. Beyond 9%, TSC did not contribute further to increasing the ECSA.

Impedance analysis was conducted to deepen the understanding and elucidate the observations in RED performance with varying amounts of TSC. The curve-fitted Nyquist plots are displayed in Figure 8A. The resistances were measured as shown in Figure 8B, and their values are summarized in Table S3. The RED cell resistance is composed of ohmic resistance (R_{ohm}), charge transfer resistance (R_{ct}), and non-ohmic resistance ($R_{non\text{-}ohm}$).[33,36] $R_{non\text{-}ohmic}$ includes the resistance of the electrical double layer, wherein ions are bound to IEM through electrostatic interaction, and the resistance of the diffusion boundary layer, which forms due to differences in ion transport between the solution and the membrane.[40] Given that all measuring conditions were constant except for the electrode, variables such as the same IEM, salinity ratio, and flow rate, the magnitude of $R_{non\text{-}ohmic}$ should be comparable in all cases. The flow rate was sufficiently high to prevent mass transfer limitations, and thus the contribution of $R_{non\text{-}ohmic}$ remained negligible. Meanwhile, R_{ohm} can be divided into contributions from the membrane, solution, and other electrical contacts such as those from the catalyst and electrode. In summary, the majority of R_{cell} originates from R_{ohm} and R_{ct}, as evidenced by a single semi-circle in Figure 8A. The inclusion of TSC in the Pt/Ti electrode resulted in a decrease in R_{ohm} from 0% to 9% TSC, attributable to the fact that the Pt layer formed was thin and compact due to initial suppression and subsequent leveling by TSC. Prior research has indicated that high electrical conductivity is obtained from the reduced grain size and uniformity when using a leveler.[60,61] An increase in R_{ohm} after 12% TSC is attributed to increased electrical resistance from over-growth of Pt and loose electrical contact due to pitting and holes. On the other hand, R_{ct} initially rose and then declined with increasing TSC content. The variation in R_{ct} closely aligned with the trend in specific capacitance as shown in Figure 7. Since R_{ct} is linked to charge transfer at the electrode surface, it decreased as a larger number of active sites with an expanded electrochemically active surface were developed.

Indicators in performance or properties generally tend to pose a certain tendency, such as a simple increase or a simple decrease and a volcano plot with the lowest or the

highest. However, in this experiment, there are results that deviate from the typical trend in the changing behavior of the maximum power density and specific capacitance according to the concentration of TSC, especially for TSC 3% electrodes. The performance of RED with TSC-based Pt/Ti electrodes increased in the following order: TSC 15% < TSC 12% < TSC 3% < TSC 0% < TSC 6% < TSC 9%. The specific capacitance of TSC-based Pt/Ti electrodes increased in the following order: TSC 3% < TSC 15% < TSC 12% < TSC 0% < TSC 6% < TSC 9%. In the case of TSC 3%, although the specific capacitance was the smallest, the RED performance was greater than that of TSC 12% or 15%. It had the smallest electrochemical active surface area, which negated the charge transfer at the electrode surface, in line with the largest R_{ct}, but the TSC content in the electrode layer was relatively small. As a result, the electrical resistance (R_{ohm}) of the electrode was slightly smaller than that of TSC 12% and 15%, which seemed to have compensated the RED performance. Conversely, TSC 12% and 15% had larger surface area than TSC 3%, but large amount of TSC decreased electrical conductivity, resulting in an occurrence of rapid polarization, as shown in j–V curve in Figure 5A. Above TSC 3%, a volcano plot of RED performance with TSC concentration was observed: a simple increase from 3% to 9% and a decrease from 9% to 15%.

The reduction behavior of Pt was monitored when TSC was used as a leveling additive. It was confirmed that the deposition rate could be controlled by varying the concentration of TSC. The physicochemical and electrochemical properties of the Pt/Ti electrodes were investigated, and the performance of the RED was measured using these electrodes. The performance enhancement was attributed to the development of electrodes with high coverage and uniformity, enlarged active surface area, and optimized microstructure. TSC is electrochemically inactive and does not influence the electrochemical reactions. However, when coordinated with a metal ion, the complex can alter the electrocatalytic properties of the metal through metal-ligand charge transfer.[62] To elucidate this, additional XPS analysis was conducted to assess whether the intrinsic properties and bonding structure of the citrate-coordinated Pt surface were altered. The XPS analysis of TSC 0%, 9%, 12% for Pt4f and O1s characteristic peaks are presented in Figure 9. All peaks were referenced to C1s (284.6 eV), deconvoluted using fitting software, and identified via data from the NIST XPS database (SRD 20, Ver. 5.0). Compared to TSC 0%, the Pt/Ti electrode with 9% TSC exhibited a higher ratio of oxygenated Pt on the surface (Figure 9A). The ratio of oxygenated Pt to metallic Pt for TSC 0% and TSC 9% was 0.64 and 0.95, respectively. This suggests that the carboxylate of citrate forms a stronger coordination with Pt^{4+} as the concentration of TSC rises. Consequently, a significant amount of Pt bonded to oxygen was distributed across the electrode surface. This substantial presence of oxygenated Pt was also corroborated by the O1s characteristic peaks observed in Figure 9B. The increasing coordination tendency of TSC with concentration may have been influenced by pH variations. Notably, TSC undergoes multistep ionization and thus coordinates effectively with metal ions as the pH level increases. This suggests that the pH of the solution rose with TSC concentration, enhancing the coordination number of carboxylate by forming tetradentate ligands. Meanwhile, the presence of Pt^{2+} on the surface indicated the concurrent reduction of Pt(IV) to Pt(0) by electrodeposition and to Pt(II) by electron-donating citrate. The charge transfer from the citrate ligand to the central Pt metal augmented the electron density of Pt, as evidenced by a lower-binding shift of $Pt4f_{7/2}$ in the Pt/Ti electrode with TSC 9% by 0.3 eV. Upon further increasing the TSC concentration to 12%, the relative quantity of oxygenated Pt on the surface was almost similar or slightly greater. However, the $Pt4f_{7/2}$ characteristic peak shifted toward higher binding energy by 0.2 eV, attributed to citrate's electron-withdrawing tendency when highly coordinated. As previously mentioned, the citrate coordinates more strongly with metal ions as its concentration increases. However, when coordination reaches a highly complex state such as tetradentate, electrons transfer from the metal to the ligand due to the π-electron resonance effect and the inductive effect of the carboxyl group. This transfer ultimately reduces the electron density on the central metal. Increased electron density near Pt, due to the coordination of citrate and charge transfer, could influence the catalytic activity of the Pt/Ti electrode, thus enhancing the Fe^{3+}/Fe^{2+} redox reaction and consequently improving the RED performance to 9% in TSC.

The long-term operation of the RED stack (5 cells) embedded with a Pt/Ti electrode fabricated using TSC 9% was conducted, as shown in Figure 10. The operating voltage was monitored over 18 h under a constant electrical load of 10 A/m^2. The voltage decay was approximately 3.2%, indicating stable operation of the RED stack with the as-prepared Pt/Ti electrode. The performance results of RED using various electrodes, such as Ir, Ru, and Pt from other literature are summarized in Figure 11. The gross power density of a RED single cell with a Pt/Ti electrode fabricated using TSC 9% was compared to the values provided. As-prepared Pt/Ti electrode in the current study exhibited a power density of 0.888 W/m^2, which is comparable and even greater than those of other Pt/Ti electrodes. This is primarily attributed to the large electrochemical surface area. Since the actual electrochemical reaction mainly occurs on the surface of the electrode and the reaction at the electrode is directly reflected in the RED performance, the surface composition, structure, and the electronic perturbation of Pt by TSC may affect

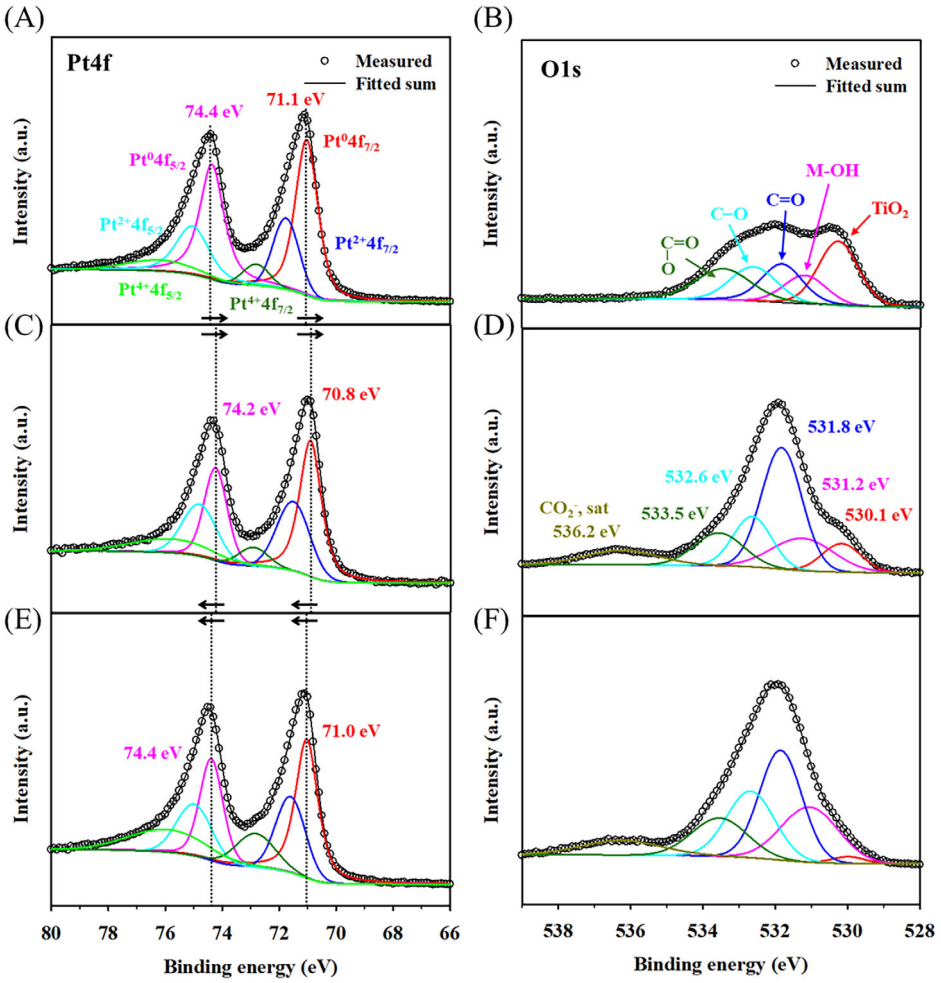

FIGURE 9 X-ray photoelectron spectroscopy of as-prepared Pt/Ti electrodes; TSC 0% (A, B), TSC 9% (C, D), and TSC 12% (E, F): Deconvoluted spectra of Pt 4f (A, C, E) and spectra of O1s (B, D, F) are presented.

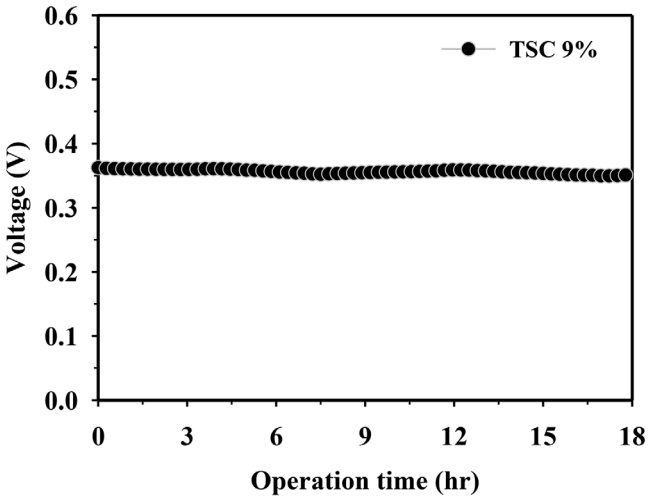

FIGURE 10 Chronopotentiometry of reverse electrodialysis stack (5 cells) embedded with Pt/Ti electrode of TSC 9% at 10 A/m^2 for 18 h for demonstrating the long-term stability of the system.

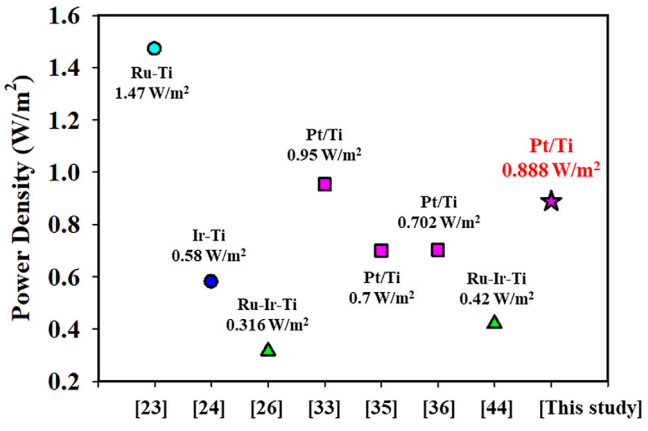

FIGURE 11 The performance comparison of reverse electrodialysis using as-prepared Pt/Ti electrodes with prior studies in terms of gross power density.

the performance as earlier mentioned in the manuscript. At this point, ion transport through the ion exchange membrane is constant because all operating conditions

including flow rate remain same. The difference in the ECSA varied directly depending on the amount of TSC added and the trend in ECSA change was very closely related to the performance behavior of RED. Although the changes in surface composition and the electronic structure of Pt showed positive correlation with the performance, but not as close as the changes in ECSA. Among the cited references, Ru-Ti electrode retained an enlarged surface and high electrical conductivity offered by Ti mesh sub-electrode and Ru, respectively, resulting in better RED performance than relevant electrodes with similar material and composition, even Pt/Ti electrode of our group. Therefore, it can be suggested that the use of Pt/Ti electrode with uniform coverage and microstructure thereby having a profoundly enlarged electrochemical active surface resulted in the improved RED performance. Compared to conventional Ir, Ru electrodes or graphite electrodes, it can be seen that the TSC-assisted fabrication of Pt/Ti is relatively simple and consumes less energy while having competitive durability and catalytic activity. However, because Pt is expensive such effort as employing TSC-based electrodeposition is needed, which helps developing electrode system with minimized usage of Pt.

4 | CONCLUSIONS

TSC-assisted ED was utilized to fabricate the Pt/Ti electrode for RED. The impact of TSC concentration on the reduction behavior of the Pt precursor and the resultant electrode was explored. Initially, TSC acted as a suppressant and subsequently as a leveler with varying concentrations. In the RED single cell application, the Pt/Ti electrode fabricated with 9% TSC exhibited the highest power density of 0.888 W/m^2—a 24% increase compared to those fabricated without TSC. FE-SEM analysis showed that TSC 9% effectively inhibited the overgrowth of Pt and facilitated the formation of a smooth Pt layer characterized by small grains and high coverage. The Pt/Ti electrode with TSC 9% displayed the most extensive active surface area, as evidenced by the highest specific capacitance on EDLC measurements and the lowest R_{ct} in the EIS analysis. The electron density of Pt increased with TSC concentration due to electrondonation through a charge transfer between Pt and citrate. However, excessive TSC that formed a stronger coordination with Pt led to electron withdrawal from Pt to citrate, due to the inductive effect of TSC. To the authors' knowledge, no prior literature describes the use of additive-based electrodeposition methods and their effects in the manufacture of electrodes for RED. The authors believe that the aforementioned results will aid in the development of highly efficient and stable electrodes for RED.

ACKNOWLEDGMENTS

The research was supported by the Basic Science Research Program through the NRF (National Research Fund) of Korea, funded by the Ministry of Science, ICT and Future Planning (2022R1C1C1013043), and by the Korea Institute of Energy Technology Evaluation and Planning (KETEP), and the Ministry of Trade, Industry & Energy (MOTIE) of the Republic of Korea (No. 20224000000080).

ORCID

Insoo Choi https://orcid.org/0000-0002-3548-2754

REFERENCES

1. Wilkinson C. Glass and a carbon-free United States: what is glass's role in the upcoming green revolution? J Am Ceram Soc. 2024;107(3):1533–42. https://doi.org/10.1111/jace.19360
2. Bao Y, Grutzeck MW, Jantzen CM. Preparation and properties of hydroceramic waste forms made with simulated Hanford low-activity waste. J Am Ceram Soc. 2005;88(12):3287–302. https://doi.org/10.1111/j.1551-2916.2005.00775.x
3. Capellán-Pérez I, Mediavilla M, de Castro C, Carpintero Ó, Miguel LJ. Fossil fuel depletion and socio-economic scenarios: an integrated approach. Energy. 2014;77:641–466. https://doi.org/10.1016/j.energy.2014.09.063
4. Alvarez-Silva OA, Osorio AF, Winter C. Practical global salinity gradient energy potential. Renew Sustain Energy Rev. 2016;60:1387–95. http://doi.org/10.1016/j.rser.2016.03.021
5. Ramon GZ, Feinberg BJ, Hoek EMV. Membrane-based production of salinity-gradient power. Energy Environ Sci. 2011;4(11):4423–34. https://doi.org/10.1039/C1EE01913A
6. Logan BE, Elimelech M. Membrane-based processes for sustainable power generation using water. Nature. 2012;488(7411):313–419. https://doi.org/10.1038/nature11477
7. Chae S, Kim H, Hong JG, Jang J, Higa M, Pishnamazi M, et al. Clean power generation from salinity gradient using reverse electrodialysis technologies: recent advances, bottlenecks, and future direction. Chem Eng J. 2023;452(P4):139482. https://doi.org/10.1016/j.cej.2022.139482
8. Hong JG, Zhang B, Glabman S, Uzal N, Dou X, Zhang H, et al. Potential ion exchange membranes and system performance in reverse electrodialysis for power generation: A review. J Memb Sci. 2015;486:71–88. http://doi.org/10.1016/j.memsci.2015.02.039
9. Ruiz-Navas D, Quiñones-Bolaños E, Sharqawy MH. Modified solution–diffusion model incorporating rotational kinetic energy in pressure retarded osmosis. Appl Sci. 2025;15(3):1312. https://doi.org/10.3390/app15031312
10. Post JW, Hamelers HVM, Buisman CJN. Energy recovery from controlled mixing salt and fresh water with a reverse electrodialysis system. Environ Sci Technol. 2008;42(15):5785–90. https://doi.org/10.1021/es8004317
11. Veerman J, Saakes M, Metz SJ, Harmsen GJ. Reverse electrodialysis: a validated process model for design and optimization. Chem Eng J. 2011;166(1):256–68. https://doi.org/10.1016/j.cej.2010.10.071
12. Mehdizadeh S, Kakihana Y, Abo T, Yuan Q, Higa M. Power generation performance of a pilot-scale reverse electrodialysis using monovalent selective ion-exchange membranes. Membranes. 2021;11(1):27. https://doi.org/10.3390/membranes11010027

13. Tedesco M, Scalici C, Vaccari D, Cipollina A, Tamburini A, Micale G. Performance of the first reverse electrodialysis pilot plant for power production from saline waters and concentrated brines. J Memb Sci. 2016;500:33–45. http://doi.org/10.1016/j.memsci.2015.10.057
14. Tristán C, Fallanza M, Ortiz I, Ibáñez R, Grossmann IE. Cost-optimal design of reverse electrodialysis process for salinity gradient-based electricity generation in desalination plants. Energy. 2024;313:134005. https://doi.org/10.1016/j.energy.2024.134005
15. Post JW, Goeting CH, Valk J, Goinga S, Veerman J, Hamelers HVM, et al. Towards implementation of reverse electrodialysis for power generation from salinity gradients. Desalin Water Treat. 2010;16(1–3):182–93. https://doi.org/10.5004/dwt.2010.1093
16. Pawlowski S, Crespo JPG, Velizarov S. Sustainable energy generation by reverse electrodialysis. Procedia Eng. 2012;44:1013–106. https://doi.org/10.1016/j.proeng.2012.08.659
17. Pattle R. Production of electric power by mixing fresh and salt water in the hydro-electric pile. Nature. 1954;174:660–660. https://doi.org/10.1038/174660a0
18. Emdadi A, Greenlee LF, Logan B. Uphill transport of sulfate and chloride ions under different operational conditions of a reverse electrodialysis (RED) stack. Chem Eng J. 2025;508:160897. https://doi.org/10.1016/j.cej.2025.160897
19. Rijnaarts T, Moreno J, Saakes M, de Vos WM, Nijmeijer K. Role of anion exchange membrane fouling in reverse electrodialysis using natural feed waters. Colloids Surfaces A: Physicochem Eng Asp. 2019;560:198–204. https://doi.org/10.1016/j.colsurfa.2018.10.020
20. Jagur-Grodzinskr J, Kramer R. Novel process for direct conversion of free energy of mixing into electric power. Ind Eng Chem Process Des Dev 1986;25(2):443–49. https://doi.org/10.1021/i200033a016
21. Güler E, van Baak W, Saakes M, Nijmeijer K. Monovalent-ion-selective membranes for reverse electrodialysis. J Memb Sci. 2014;455:254–70. http://doi.org/10.1016/j.memsci.2013.12.054
22. Rosentreter H, Scope C, Oddoy T, Lerch A, Meier-Haack J. Monovalent selective ion exchange membranes: A review on preparation processes, applications, performance criteria and sustainability aspects. Desalination. 2025;599: 118412. https://doi.org/10.1016/j.desal.2024.118412
23. Liu J, Liu M, Wang J, Feng Z, Li X, Cao M. Highly conductive anti-fouling anion exchange membranes for power generation by reverse electrodialysis. J Power Sources. 2024;598:234176. https://doi.org/10.1016/j.jpowsour.2024.234176
24. Hong JG, Park TW. Electrochemical characterizations and reverse electrodialysis performance of hybrid anion exchange membranes for salinity gradient energy. J Electroanal Chem. 2018;817:134–40. https://doi.org/10.1016/j.jelechem.2018.04.005
25. Güler E, Elizen R, Saakes M, Nijmeijer K. Micro-structured membranes for electricity generation by reverse electrodialysis. J Memb Sci. 2014;458:136–48. http://doi.org/10.1016/j.memsci.2014.01.060
26. Karakoç E, Güler E. Comparison of physicochemical properties of two types of polyepichlorohydrin-based anion exchange membranes for reverse electrodialysis. Membranes. 2022;12:257. https://doi.org/10.3390/membranes12030257
27. Mujahid M, Wang C, Farooq MU, Feng L, Qiu Y, Li J, et al. Synergistic optimization of membrane distillation-reverse electrodialysis for sustainable desalination and salinity gradient power generation. Sep Purif Technol. 2025;360:130953. https://doi.org/10.1016/j.seppur.2024.130953
28. Wu B, Zhang Q, Wu H, Tian Q, Chai W, Zhang M, et al. Integrated membrane process of tubular ultrafiltration-nanofiltration-electrodialysis-reverse osmosis for treating fracturing flowback fluid. J Clean Prod. 2024;469:142995. https://doi.org/10.1016/j.jclepro.2024.142995
29. Mehdizadeh S, Yasukawa M, Abo T, Kakihana Y, Higa M. Effect of spacer geometry on membrane and solution compartment resistances in reverse electrodialysis. J Memb Sci. 2019;572:271–80. https://doi.org/10.1016/j.memsci.2018.09.051
30. Kim HK, Lee MS, Lee SY, Choi YW, Jeong NJ, Kim CS. High power density of reverse electrodialysis with pore-filling ion exchange membranes and a high-open-area spacer. J Mater Chem A. 2015;3(31):16302–6. https://doi.org/10.1039/C5TA03571F
31. Gurreri L, Tamburini A, Cipollina A, Micale G, Ciofalo M. CFD prediction of concentration polarization phenomena in spacer-filled channels for reverse electrodialysis. J Memb Sci. 2014;468:133–48. http://doi.org/10.1016/j.memsci.2014.05.058
32. Jalili Z, Pharoah JG, Burheim OS, Einarsrud KE. Temperature and velocity effects on mass and momentum transport in spacer-filled channels for reverse electrodialysis: A numerical study. Energies. 2018;11(8):2028. http://doi.org/10.3390/en11082028
33. Choi I, Han JY, Yoo SJ, Henkensmeier D, Kim JY, Lee SY, et al. Experimental investigation of operating parameters in power generation by lab-scale reverse electro-dialysis (RED). Bull Korean Chem Soc. 2016;37(7):1010–19. https://doi.org/10.1002/bkcs.10810
34. Chon K, Jeong N, Rho H, Nam JY, Jwa E, Cho J. Fouling characteristics of dissolved organic matter in fresh water and seawater compartments of reverse electrodialysis under natural water conditions. Desalination. 2020;496:114478. https://doi.org/10.1016/j.desal.2020.114478
35. Simões C, Saakes M, Brilman D. Toward redox-free reverse electrodialysis with carbon-based slurry electrodes. Ind Eng Chem Res. 2023;62(3):1665–75. https://doi.org/10.1021/acs.iecr.2c03567
36. Jeong J, Song H, Choi I. Electrochemical analysis on how structural and compositional modification of electrode affects power generation in reverse electrodialysis. Korean J Chem Eng. 2021;38(1):170–78.
37. Jang J, Kang Y, Han JH, Jang K, Kim CM, Kim IS. Developments and future prospects of reverse electrodialysis for salinity gradient power generation: influence of ion exchange membranes and electrodes. Desalination. 2020;491:114540. https://doi.org/10.1016/j.desal.2020.114540
38. Simões C, Pintossi D, Saakes M, Borneman Z, Brilman W, Nijmeijer K. Electrode segmentation in reverse electrodialysis: improved power and energy efficiency. Desalination. 2020;492:114604. https://doi.org/10.1016/j.desal.2020.114604
39. Akter M, Park J-S. Fouling and mitigation behavior of foulants on ion exchange membranes with surface property in reverse electrodialysis. Membranes. 2023;13(1):106. https://doi.org/10.3390/membranes13010106
40. Song H, Choi I. Unveiling the adsorption mechanism of organic foulants on anion exchange membrane in reverse electro-

dialysis using electrochemical methods. J Appl Electrochem. 2023;53(5):1043–56. https://doi.org/10.1007/s10800-022-01816-5
41. Burheim OS, Seland F, Pharoah JG, Kjelstrup S. Improved electrode systems for reverse electro-dialysis and electro-dialysis. Desalination. 2012;285:147–52. http://doi.org/10.1016/j.desal.011.09.048
42. Flox C, Skoumal M, Rubio-Garcia J, Andreu T, Morante JR. Strategies for enhancing electrochemical activity of carbon-based electrodes for all-vanadium redox flow batteries. Appl Energy. 2013;109:344–51. http://doi.org/10.1016/j.apenergy.2013.02.001
43. McCreery RL, McDermott MT. Comment on electrochemical kinetics at ordered graphite electrodes. Anal Chem. 2012;84(5):2602–5. https://doi.org/10.1021/ac2031578
44. Wu X, Zhang Y, Sun D, Lv Y, Liu M, Zhu X. Enhancement of power density and hydrogen productivity of the reverse electrodialysis process by optimizing the temperature gradient between the working solutions. Chem Eng J. 2024;498:155385. https://doi.org/10.1016/j.cej.2024.155385
45. Xiao X, Yin H, Chen J, Zhu C. Synthesis of $Cu_{2-x}S$ electrocatalysts with different stoichiometric numbers by electrodeposition and heat posttreatment. J Am Ceram Soc. 2024;107:4331–41. https://doi.org/10.1111/jace.19710
46. Ye W, Guo X, Ma T. A review on electrochemical synthesized copper-based catalysts for electrochemical reduction of CO_2 to C2+ products. Chem Eng J. 2021;414:128825. https://doi.org/10.1016/j.cej.2021.128825
47. Zeng TW, Yen SC. Effects of additives in an electrodeposition bath on the surface morphologic evolution of electrodeposited copper. Int J Electrochem Sci. 2021;16(2):210245. https://doi.org/10.20964/2021.02.40
48. Kim SK, Josell D, Moffat TP. Electrodeposition of cu in the PEI-PEG-Cl-SPS additive system. J Electrochem Soc. 2006;153(9):C616. https://doi.org/10.1149/1.2216356
49. Liu L, Bu Y, Sun Y, Pan J, Liu J, Ma J, et al. Trace bis-(3-sulfopropyl)-disulfide enhanced electrodeposited copper foils. J Mater Sci Technol. 2021;74:237–45. https://doi.org/10.1016/j.jmst.2020.10.019
50. Schmitt KG, Schmidt R, Von-Horsten HF, Vazhenin G, Gewirth AA. 3-mercapto-1-propanesulfonate for Cu electrodeposition studied by in situ shell-isolated nanoparticle-enhanced Raman spectroscopy, density functional theory calculations, and cyclic voltammetry. J Phys Chem C. 2015;119(41):23453–62. https://doi.org/10.1021/acs.jpcc.5b06274
51. Wang Y, Zheng X, Li X. Effect of polyethylene glycol molecular weight on the electrodeposition of nanostructured nickel. Appl Surf Sci. 2023;623:156886. https://doi.org/10.1016/j.apsusc.2023.156886
52. Lari Baghal SM, Amadeh A, Heydarzadeh Sohi M, Hadavi SMM. The effect of SDS surfactant on tensile properties of electrodeposited Ni-Co/SiC nanocomposites. Mater Sci Eng A. 2013;559:583–90. http://doi.org/10.1016/j.msea.2012.08.145
53. Fang JS, Wu JL, Wang SM, Hsu CH, Cheng YL, Chen GS. Influence of trisodium citrate on the Cu electrodeposition by sequential underpotential deposition of Pb and surface-limited redox replacement of Cu. Int J Electrochem Sci. 2018;13(8):7466–77. https://doi.org/10.20964/2018.08.70
54. Agawane GL, Shin SW, Moholkar AV, Gurav KV, Yun JH, Lee JY, et al. Non-toxic complexing agent tri-sodium citrate's effect on chemical bath deposited ZnS thin films and its growth mechanism. J Alloys Compd. 2012;535:53–61. http://doi.org/10.1016/j.jallcom.2012.04.073
55. Hwang J, Chun J. Microwave-assisted solvothermal synthesis of sodium metal fluoride (Na_xMF_y) nanopowders. J Am Ceram Soc. 2019;102:6475–79. https://doi.org/10.1111/jace.16702
56. Wei G, Ge H, Huang L, Wu Q, Wang X, Huang L. Influence of complexing agent on the electrodeposited Co-Pt-W magnetic thin films. Appl Surf Sci. 2008;254(11):3425–30. https://doi.org/10.1016/j.apsusc.2007.11.038
57. Lackovic K, Johnson BB, Angove MJ, Wells JD. Modeling the adsorption of citric acid onto Muloorina illite and related clay minerals. J Colloid Interface Sci. 2003;267(1):49–59.
58. Kumar KS, Biswas K. Effect of thiourea on grain refinement and defect structure of the pulsed electrodeposited nanocrystalline copper. Surf Coatings Technol. 2013;214:8–18. http://doi.org/10.1016/j.surfcoat.2012.10.018
59. Sogaard M, Odgaard M, Skou EM. An improved method for the determination of the electrochemical active area of porous composite platinum electrodes. Solid State Ionics. 2001;145(1–4):31–35. https://doi.org/10.1016/S0167-2738(01)00908-0
60. Eiler K, Suriñach S, Sort J, Pellicer E. Mesoporous Ni-rich Ni–Pt thin films: electrodeposition, characterization and performance toward hydrogen evolution reaction in acidic media. Appl Catal B Environ. 2020;265:118597. https://doi.org/10.1016/j.apcatb.2020.118597
61. Zheng L, He W, Zhu K, Wang C, Wang S, Hong Y, et al. Investigation of poly (1-vinyl imidazole co 1, 4-butanediol diglycidyl ether) as a leveler for copper electroplating of through-hole. Electrochim Acta. 2018;283:560–67. https://doi.org/10.1016/j.electacta.2018.06.132
62. Franco-Ulloa S, Tatulli G, Bore SL, Moglianetti M. Pompa PP, Cascella M, et al. Dispersion state phase diagram of citrate-coated metallic nanoparticles in saline solutions. Nat Comm. 2020;11:5422. https://doi.org/10.1038/s41467-020-19164-3

SUPPORTING INFORMATION

Additional supporting information can be found online in the Supporting Information section at the end of this article.

How to cite this article: Kwon E, Lee D, Choi I. The effect of organic additive on electrochemical fabrication of microstructured electrode for reverse electrodialysis. J Am Ceram Soc. 2025;108:e20570. https://doi.org/10.1111/jace.20570